Estimates of cloud vertical structure and water amount over tropical oceans using VIRS and TMI data

Shu-peng Ho

Atmospheric Chemistry Division, National Center for Atmospheric Research, Boulder, Colorado, USA

Bing Lin and Patrick Minnis

Atmospheric Sciences, NASA Langley Research Center, Hampton, Virginia, USA

Tai-Fang Fan

SAIC, One Enterprise Parkway, Hampton, Virginia, USA

[1]   A microwave, visible and infrared (MVI) method was applied to coincident, collocated Tropical Rainfall Measuring Mission (TRMM) Microwave Imager (TMI) and VIRS (Visible and Infrared Scanner) data collected from January to August 1998 to estimate the cloud vertical structure and water path over tropical oceans. The derived quantities include the liquid water path (LWP), ice water path (IWP), total water path (WP), the frequencies of single-layer and overlapping nonprecipitating clouds, and the cloud top-height, base-height and thickness for single-layered water clouds. LWP data retrieved from TMI measurements were compared with global and regional LWP retrieved from VIRS for warm nonprecipitating clouds for different seasons. The global mean difference between TMI LWP and VIRS LWP is less than 0.01 mm and varies with season. For cold clouds, the TMI LWP is only 25–30% of the VIRS WP. In these cases, the ice clouds observed by VIRS overlap liquid water clouds. This result is similar to that from an earlier study, however, the well-matched TMI and VIRS data provide more accurate instantaneous estimates than were previously possible. The assumption, that the cloud is entirely ice, used to compute IWP introduces some errors in the WP because of cloud overlapping. However, the difference between IWP estimated for all TMI FOVs containing only ice-phase VIRS pixels and the IWP estimated from the difference between the VIRS WP and TMI LWP is less than 10%. This result suggests that IWP is independent of the lower-level clouds for nonprecipitating systems. For warm single-layered clouds, the estimated low-cloud-base altitudes (∼800m) and thicknesses (between 800 m to 1000 m) are, on average, very close to low-cloud results derived from combined surface and upper-air observations. The frequency of overlapped nonprecipitating clouds over ocean was about 4%, 16% and 38% for low, middle, and high clouds, respectively. The results clearly demonstrate the potential for enhanced monitoring of maritime clouds using infrared, solar, and microwave imagers on the same platform.   *INDEX TERMS:* 1655 Global Change: Water cycles (1836); 3359 Meteorology and Atmospheric Dynamics: Radiative processes; 3360 Meteorology and Atmospheric Dynamics: Remote sensing; 3399 Meteorology and Atmospheric Dynamics: General or miscellaneous; *KEYWORDS:* Cloud, overlapped cloud, LWP, TMI, VIRS

1. Introduction

[2]   Clouds are very important regulators of the hydrological cycle and the energy balance of the earth. Cloud vertical structure, including cloud water and ice amounts, cloud top and base heights, cloud layer thickness, and cloud overlapping, affect both shortwave and longwave radiation and the vertical distributions of latent heat release [*Webster and Stephens*, 1984]. Accurate global cloud liquid/ice water path (LWP and IWP) retrievals and the knowledge of the temporal and spatial distributions of multilayered clouds are critical for understanding the Earth's climate.

[3]   Most of the current information on the global distribution of cloud vertical structure, including top and bases heights, the co-occurrence of different type clouds, the

seasonal variations and the geographical distributions of multilayered clouds is based on observations of land weather stations and from ships in the oceans [*Hahn et al.*, 1982; *Warren et al.*, 1985, 1988]. However, when lower clouds are present or during the night, surface observers may not be able to identify cirrus and altostratus/altocumulus clouds [*Poore et al.*, 1995]. Surface observations do not provide cloud top height/pressure and optical thickness information either. Because of the sparse geographic coverage of observation stations, surface observations can only provide the large-scale (15° latitude × 30° longitude over ocean and 5° × 5° over land, *Hahn et al.* [1982, 1984]) variation of cloud vertical distributions. Although surface observers report that multilayered clouds occur approximately 40% of the time over large areas of the Intertropical and Southern Pacific Convergence Zones (ITCZ and SPCZ) [*Warren et al.*, 1985, 1988], the results are highly uncertain for a particular season and year and do not provide the quantitative information, such as cloud water path, needed to compare with climate model calculations. Furthermore, the surface observations (including radiosonde observations) do not provide cloud optical properties, such as cloud optical depth and effective droplet size that are essential for quantifying the role of clouds in the climate system [*Han et al.*, 1994]. Such quantities can only be derived over extensive areas using satellite data. More independent and objective observations are needed to verify the cloud vertical structures observed from surface [*Poore et al.*, 1995]. With higher spatial and temporal coverage, satellite observations of radiances at solar and infrared wavelengths yield near-global distributions of cloud amount, optical depth, temperature, and height [*Rossow and Schiffer*, 1991] as well as effective droplet size [e.g., *Han et al.*, 1994], phase, and ice crystal size [e.g., *Minnis et al.*, 1998]. These cloud parameters are usually retrieved with an assumption that each cloudy pixel contains a single-layer cloud. Although a few techniques have been developed for detecting multilayered clouds from passive remote sensing [e.g., *Ou et al.*, 1996; *Baum and Spinhirne*, 2000], none have been applied over extensive areas or time periods because much additional effort is required to make such infrared-solar methods globally robust. Additionally, such methods are limited to detecting multilayered cloud systems consisting of thin cirrus over extensive low cloud decks. Multilayered clouds can be determined more definitively from active sensors such as airbone lidar [*Sassen*, 1991; *Platt et al.*, 1994] and surface-based radar measurements [*Kropfli et al.*, 1995] for a wider range of cloud conditions. However, such measurements are constrained to a particular site or to certain field experiments [e.g., *Uttal et al.*, 1995; *Wang et al.*, 1999, 2000]. *Lin et al.* [1998b] demonstrated that a combination of MW, VIS, and IR data could be used together to determine the distribution of overlapped (two separate cloud layers in this study) ice-over-water clouds over oceans.

[4] LWP can be derived directly from microwave data over oceans while VIS-IR methods estimate LWP indirectly through the retrievals of optical depth and effective particle size. For single-layer water clouds, VIS-IR and MW methods should provide consistent LWP estimates over oceans. In multilayered cloud cases, especially when the upper layer clouds are thick enough, the VIS-IR radiances are primarily sensitive to the upper cloud layer, and the VIS-IR methods generally cannot distinguish lower-level water clouds from high-level overcast, thick ice/water clouds. Thus over oceans, the VIS-IR and MW techniques can be combined to determine the presence of water clouds below the ice clouds.

[5] In this study, the MVI (MW, VIS, and IR) method developed for a combination of SSM/I (Special Sensor Microwave Imager) and Meteosat data by *Lin et al.* [1998b] is adapted and applied to data collocated from the *TRMM* Microwave Imager (TMI) and the Visible and Infrared Scanner (VIRS) on the Tropical Rainfall Measuring Mission (*TRMM*) satellite during January to August of 1998 to estimate LWP for all types of clouds. To avoid the uncertainties in LWP retrieved from MW data in precipitating clouds, only nonprecipitating clouds are considered. Because TMI and VIRS are on the same platform, the temporal matches (∼0.04 sec) of the VIRS cloud products and the TMI measurements are much closer than those between SSM/I and ISCCP (International Satellite Cloud Climatology Project) data (∼1.5 hours, see *Lin and Rossow* [1994]) and those between SSM/I and Meteosat (∼0.5 hour, see *Lin et al.* [1998b]). Furthermore, a technique to explicitly retrieve optical depth and particle size of ice clouds was applied to the VIRS measurements [*Minnis et al.*, 1995] yielding a different measure of total water path than that from *Lin and Rossow* [1996]. The TMI LWP retrievals are compared to the corresponding results derived from VIRS. This consistency check between the VIRS and TMI LWP values constitutes a form of validation and should lend confidence to the LWP values determined over marine areas. On the basis of the agreement between the TMI and VIRS LWP values, this paper derives the cloud-top and base heights and cloud thickness, cloud ice water path and frequencies of overlapped clouds for nonprecipitating cloud under overcast conditions over the tropical oceans.

2. Data and Microwave Retrieval Method

2.1. Data

[6] Launched in late 1997, *TRMM* is in a 350-km circular orbit with a 35° degree inclination angle [*Kummerow et al.*, 1998]. This orbit produces a sequence of Equatorial crossing times that cover the full diurnal cycle in about 46 days. Thus measurements can be taken over the full range of solar zenith angles over a given region twice in a season. The *TRMM* data used here were taken between 1 January and 31 August 1998.

[7] VIRS is a five-channel imager that measures radiances at wavelengths 0.65 (visible, VIS), 1.64, 3.75 (solar infrared, SIR), 10.8 (infrared, IR), and 12.0 μm. The VIRS 2-km radiance data were used to retrieve cloud fraction, phase, optical depth, effective particle size, and liquid (LWP_V) or ice water path (IWP_V) as well as sea surface temperature SST and cloud-top temperature Tc and height z for the Clouds and Earth's Radiant Energy System (CERES) project [*Wielicki et al.*, 1998]. This study uses the CERES VIRS Edition-1 cloud products [*Minnis et al.*, 1999].

[8] TMI is a nine-channel, passive MW radiometer measuring radiances at 10.65, 19.35, 21.3, 37.0 and 85.5 GHz. All wavelengths have both vertical (V) and horizontal (H)

polarization channels except for 21.3 GHz that only has a vertical polarization channel. TMI scans conically with an incident angle of 52.8° at the sea surface. The scanned sector yields a swath width of ~760 km. The 85.5- and 37-GHz instantaneous footprints are 6.9 km (down-track direction) by 4.6 km (cross-track direction) and 16 km by 9.7 km, respectively. The TMI antenna temperature was converted to the brightness temperature Tb with the method of *Wentz* [1998]. Although the TMI Tb was calibrated against the dark universe background and on-board microwave source, small biases still exist [*Wentz*, 1998]. Furthermore, there are small uncertainties in theoretical calculations of water vapor and liquid water absorption coefficients [*Lin et al.*, 2001] and retrieved geophysical parameters. Thus an extra microwave radiance calibration is needed for quantitative data analysis.

2.2. Data Matching

[9] Since TMI has larger footprints than VIRS, the VIRS cloud products were convolved with the TMI data to produce VIRS equivalent cloud properties at TMI footprints. Each VIRS pixel is classified as either ice or water phase. Thus the VIRS total water path WP_V is equal to the average LWP_V or IWP_V for TMI footprints containing only liquid or ice water clouds, respectively. If both phases are present, then WP_V is the weighted average of LWP_V and IWP_V. Because TMI and VIRS are on the same platform, the temporal and spatial mismatches of the VIRS cloud products and TMI footprints are negligible. The TMI-VIRS results were averaged into 1° latitude-longitude grids to reduce the retrieval uncertainties in both data sets, especially the uncertainties of ~0.04 mm in the MW LWP (LWP_T).

2.3. Microwave Retrieval Method

[10] The plane-parallel MW radiation transfer model (MWRTM) of *Lin et al.* [1998a] was used to simulate Tb for all TMI channels. Hereafter, the subscripts for Tb at each channel denote the frequency in GHz and the polarization. A lookup table (LUT) was built for various atmospheric conditions including a range of cloud temperatures (Tc), LWP_T, atmospheric water vapor, near-surface wind speed (WS), column water vapor (CWV), and sea surface temperature (SST). Tb_{37H} is used to estimate LWP. Since the water absorption coefficients increase with decreasing temperature, Tb_{37H} increases with cloud height. Conversely, the atmospheric transmittance at 85 GHz is small so that the variation of Tb_{85} with LWP depends on the competition between cloud water temperature (Tw) and upwelling microwave radiation at cloud base. On the basis of MWRTM simulations, unique solutions for LWP_T and Tw can be retrieved simultaneously using Tb_{37H} and Tb_{85V} measurements.

[11] To estimate WS and SST from TMI measurements, empirical coefficients were generated from the linear regressions between matched TMI Tb's and in-situ buoy data under nonprecipitating conditions. The linear regression for these channels in units of m/sec is

$$WS = 146.36 + 0.5752 \, Tb_{10H} - 0.08165 \, Tb_{19H}$$

$$-1.3397 \, Tb_{37V} + 0.67 \, Tb_{37H} \tag{1}$$

where surface wind speeds correspond to 5 or 10 m above the sea surface. Owing to the strong correlation between
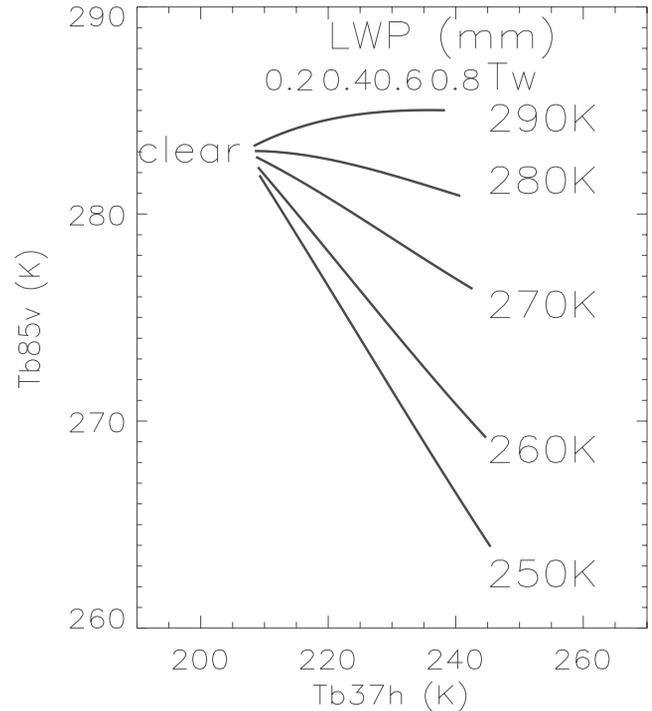

Figure 1. Microwave radiative transfer simulation of Tb_{37H} and Tb_{85V} for liquid-water clouds for Tw equals to 290 (K) (top curve), 280(k), 270 (K), 260(K) and 250 (K) (bottom curve) and corresponding LWP is from 0 mm (clear) to 0.8 mm.

SST and CWV, Tb_{21} is used in the linear regression expression of SST (°C):

$$SST = -223.49 + 2.1094 \, Tb_{10V} - 0.4187 \, Tb_{10H}$$

$$-1.0339 \, Tb_{19V} + 0.57659 \, Tb_{21V} \tag{2}$$

Compared to in-situ buoy data, the bias and standard deviation errors at TMI pixel level for these estimations are 0.56 and 1.89 K for SST and 0.8 m/s and 1.5 m/s for wind speeds, respectively. The bias and the standard deviation errors between 1°-gridded averaged TMI SST and VIRS SST are 0.11 K and 0.98 K, respectively.

[12] To use the MWRTM in the retrievals of LWP and Tw, the bias between the simulated and TMI-observed Tb's are determined for clear-sky cases only. TMI pixels containing less than 0.5% VIRS cloudy pixels are treated as clear pixels. The retrieved SST, WS, and CWV for these pixels are used in the MWRTM to simulate the clear-sky Tb, which is then used to compute the bias relative to the observations. Because 21 GHz is located at a water vapor absorption wing, Tb_{21V} is used to retrieve CWV. Assuming that the cloudy bias is the same as the adjacent clear bias, the clear TMI biases are applied to those adjacent cloudy TMI footprints. Thus the clear-sky calibration correction minimizes LWP retrieval errors in cloudy conditions caused by uncertainties in SST, WS, and CWV. For each cloudy pixel, LWP and Tw can be retrieved from the LUT simultaneously using SST, WS, CWV, and bias-corrected values of Tb_{37H} and Tb_{85V} (Figure 1). From simulations, *Lin et al.* [1998a]
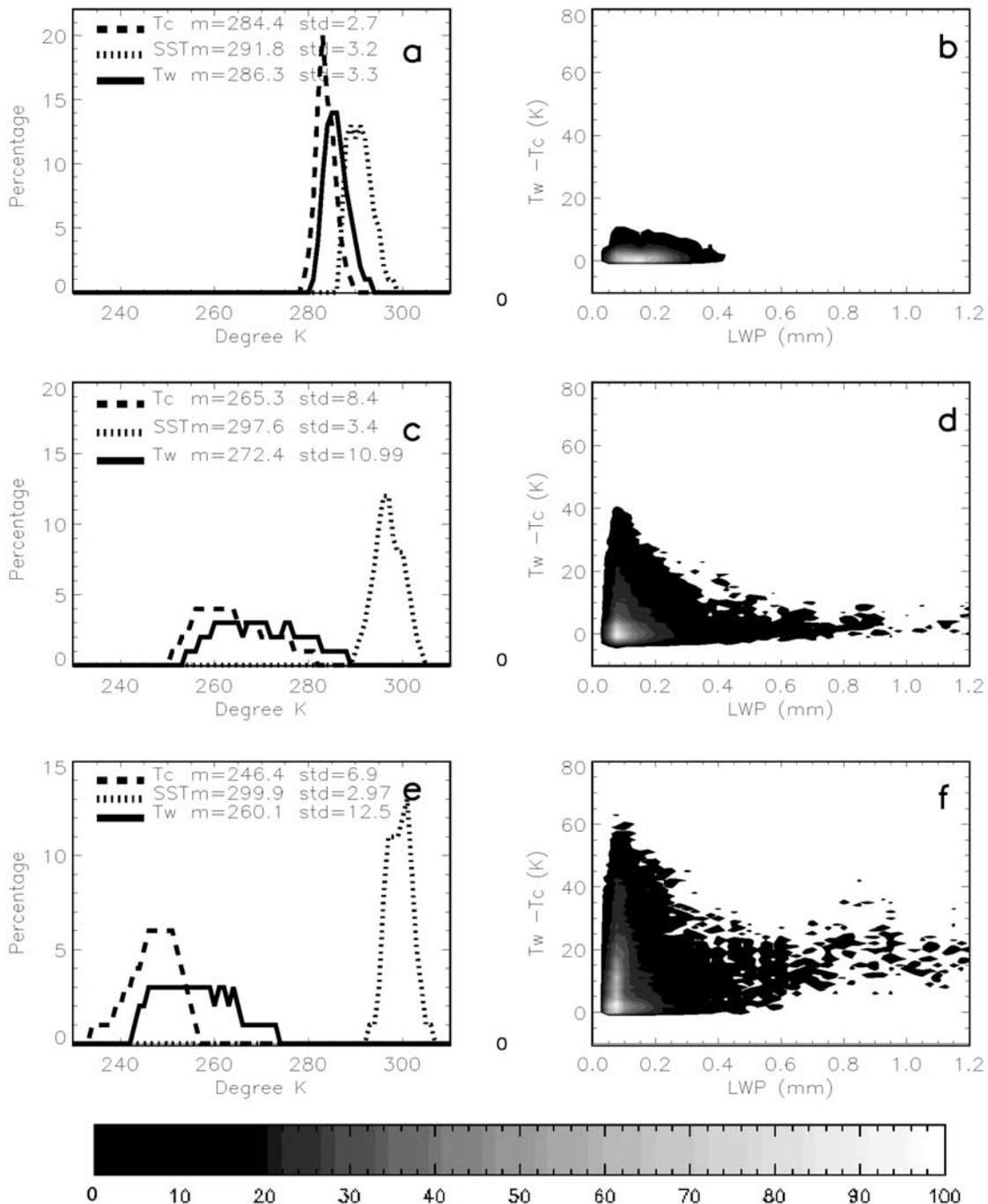
Figure 2. The probability distributions (relative frequency) of the Tw and Tc for (a) low (z < 2 km), (c) middle (2 < z < 6 km), and (e) high (z > 6 km) and their corresponding Tw − Tc and LWP$_T$ 2-D relative frequency (in%) for (b) low, (d) middle and (f) high overcast nonprecipitating clouds over midlatitude ocean (20° to 38°N) from July 1998.

showed that the simultaneous retrieval yields a bias error of about ±0.01 mm in *LWP*.

3. Detection of Overlapped Clouds

[13] The value of *Tw* retrieved from TMI data represents a mean water temperature of an integrated cloud column [*Lin et al.*, 1998] whereas the *Tc* derived from VIRS data represents the temperature near the top of the cloud for optically thick clouds [*Minnis et al.*, 1993]. Therefore when the difference, $\Delta Twc = Tw - Tc$, is significantly positive, it is likely that the observed system consists of overlapped clouds.

[14] Samples of matched cloud products over midlatitude ocean (20° to 38° N) in July 1998 are used to demonstrate the vertical structure of clouds and find the criteria to determine cloud overlapping. Figure 2 shows the probability distributions of *Tw* and *Tc* for low (z ≤ 2 km; a), middle

($2 < z \leq 6$ km; c), and high ($z > 6$ km; e) clouds and frequency distribution plots of the corresponding values of ΔTwc and LWP_T (b, d, f). Under overcast conditions, the relative fractions for the three types of the clouds were 34, 38, and 28%, respectively. To reduce the instantaneous uncertainties, only scenes with $LWP_T > 0.04$ mm are used [*Lin et al.*, 1998a]. For low clouds, the mean value of Tw is 286.3 K with a standard deviation of 3.3 K while the mean Tc is about 284.4 K with a slightly smaller standard deviation (2.7 K; Figure 2a). On average, Tw and Tc are about 5.5 and 7.5 K colder than SST, respectively. Cloud water temperature is 2 K warmer than Tc and is 2-K less than the average of SST and Tc, indicating that the clouds more likely are single layered (or narrowly separated if they are multilayered systems). Since Tw represents the integrated effective MW liquid water temperature, with the lapse rate $\Gamma = -7.1$ K/km of the standard midlatitude summer atmospheres [*McClatchey et al.*, 1972] the thickness of most low clouds, stratus (St) and stratocumulus (Sc), in northern hemisphere summer should be about 563 m which is close to midlatitude low cloud thickness ($\sim$700 m) estimated from radiosonde data [*Wang and Rossow*, 1995]. Cloud base height, which can also be estimated from the differences, $SST - Tw$ and ΔTwc, is about 500–600m, a range that is also very close to observations [*Poore et al.*, 1995]. The vertical distribution of low clouds can be seen more clearly from frequency distribution plots of ΔTwc and LWP_T (Figure 2b). Cloudy pixels with negative ΔTwc values are mainly due to the uncertainty in the Tw retrievals (Note: for the current 1° gridded data the uncertainty is $\sim$3 K). To reduce the Tw uncertainties in this comparison, values of LWP_T less than 0.04 mm are excluded resulting in the rejection of about 20% of the cloud samples. As mentioned above, the mean global low-level cloud thickness is about 700m, a value that requires ΔTwc to be at least 3 K to separate the two cloud layers. Considering that the retrieval uncertainty of Tw is around 5 K for an individual scene, ΔTwc must be larger than 8 K to confidently detect two separate cloud layers [*Lin et al.*, 1998b]. Thus cloudy pixels with ΔTwc less than 8 K are assumed to be single-layer clouds in midlatitude regions. For single-layer clouds, cloud thickness and cloud top and base heights are estimated from the values of Tw, Tc, SST and Γ, i.e.,

$$H_{CLD} = -2\Delta Twc/\Gamma. \quad (3)$$

$$z_T = -(SST - Tc)/\Gamma. \quad (4)$$

$$z_B = -\{SST - (Tw + \Delta Twc)\}/\Gamma. \quad (5)$$

where H_{CLD} is the single-layered water cloud thickness in km, and z_T and z_B are the cloud top and base heights, respectively.

[15] For middle clouds (Figures 2c and 2d), the mean Tw is 272.4 K with a standard deviation of 11.0 K. The mean Tc is 265.3 K with a standard deviation of 8.4 K, where the SST is 297.6 K. The warmest clouds with more or less uniform Tw distribution are marine boundary layer Stratus (St) and Stratocumulus (Sc). The much greater value of ΔTwc in midlevel clouds compared to that for the low clouds strongly suggests that liquid water clouds occurred below some of the water/ice clouds. On the basis of the midlatitude cloud thickness estimate ($\sim$1200 m) from radiosonde data [*Wang and Rossow*, 1995], 5 K corresponds to the average difference between the cloud-top and cloud-center temperatures. Considering the Tw retrieval uncertainty and the center-top temperature difference, ΔTwc must exceed 10 K for a midlevel cloud to be considered to consist of two different cloud layers.

[16] For high clouds (Figures 2e and 2f), on average, Tw (260.1 K) is much greater than Tc (246.4 K). For these clouds, Tc falls in a range between 220 K and 260 K while Tw varies from 240 to 290 K with most values below 273 K. Thus most of the liquid water clouds in these high-cloud systems are composed of super-cooled droplets. Ground observations [*Hahn et al.*, 1982] show that in the Tropics, cirrus clouds most often overlap altostratus (As), cumulus and cumulonimbus underneath and less often overlap St and Sc. The large Tw variation indicates more vertical distribution exists below high clouds than those below low clouds and midlevel clouds. This greater variation is to be expected given the greater atmospheric thickness below high clouds. To account for the instantaneous uncertainties in Tw and the finite thickness of the clouds, it is assumed that the VIRS high clouds overlap a lower level cloud if $\Delta Twc \geq 15$ K. In summary, it is assumed that the VIRS low, middle, and high clouds overlap a lower-level cloud if $\Delta Twc \geq 8$K, ≥ 10 K, or ≥ 15 K, respectively.

[17] From the frequency distribution plots of ΔTwc and LWP_T in Figures 2b, 2d, and 2f, it was found that overlapped clouds occurred about 1, 24 and 35% of the time, respectively, for the VIRS low, middle, and high clouds in the northern hemisphere (20° to 38° N) during summer 1998. Using collocated Meteosat and SSM/I data taken during 1–28 June 1992, over the Atlantic Stratocumulus Transition Experiment (ASTEX) region (25° to 40° N, 330 E to 345 E), *Lin et al.* [1998b] found cloud overlapping frequencies for overcast low, middle, and high of approximately 0, 19 and 36%. In-situ 8-mm Doppler radar data yielded 0, 21 and 36% overlapping, respectively, for almost the whole month of June 1992 over the island of Porto Santo in the eastern part of the ASTEX domain [*Uttal and Frisch*, 1994]. The cloud overlapping frequencies derived here from June 1998 *TRMM* data for the ASTEX region for overcast low, middle and high clouds are about 2, 15, and 33%, respectively (not shown). The similar results from these three independent data sets show statistical consistency of the MVI technique and the criteria used to detect overlapping clouds. In this study, the atmospheric climatological lapse rates for tropical, midlatitude summer, and midlatitude winter [*McClatchey et al.*, 1972] are used for corresponding regions during different seasons to compute the cloud thickness and top and base heights (equations (3), (4), and (5)) as well as for detecting overlapped clouds.

4. Consistency of Global LWP

4.1. The Bias Correction of TMI Brightness Temperatures

[18] The accuracy of the bias correction method can be tested by using the bias-corrected Tb_{37V} and Tb_{85H} to

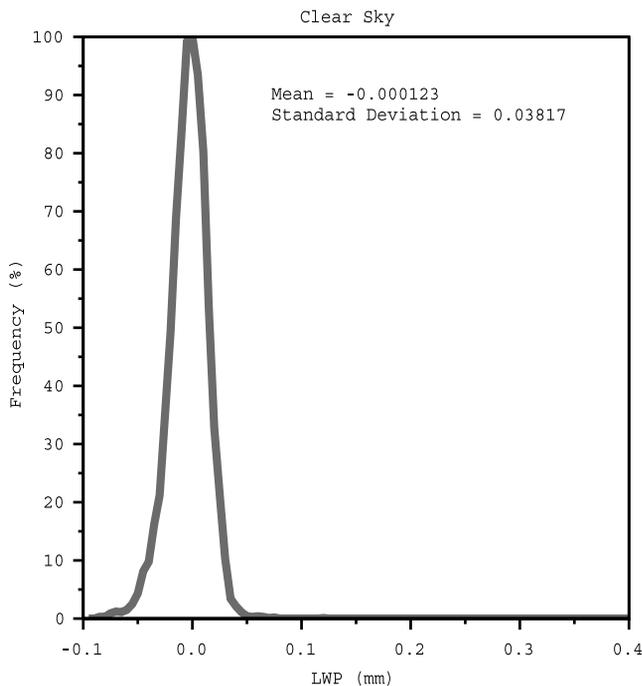Clear Sky

Mean = -0.000123
Standard Deviation = 0.03817

Figure 3. The histogram of retrieved LWP for clear skies.

retrieve LWP in clear-sky conditions. The histogram of LWP_T for clear skies shows that the mean LWP_T is very close to zero (Figure 3), indicating a correct bias adjustment. The small standard deviation (~0.04 mm) of the LWP distribution is mainly due to uncertainties in the inputs (discussed in section 6).

4.2. Global Comparisons of LWP_T and LWP_V for Warm Nonprecipitating Clouds

[19] To ensure consistency between the two data sets, LWP_T is compared with LWP_V. Under general conditions (including precipitation and ice clouds), because of the spectral differences between the TMI and VIRS measurements and the retrieval algorithm differences, LWP_T should not necessarily agree with LWP_V. To minimize the occurrence of ice-cloud contamination in the VIRS retrievals, only warm ($Tc > 273.16K$), nonprecipitating, overcast clouds with more than 30 VIRS pixels matched to TMI footprints are used to examine the consistency between the two retrievals. In this case, LWP_T should be nearly the same as LWP_V. Clouds are defined as precipitating if $[Tb_{37V} - Tb_{37H}] < 37$ K [Lin and Rossow, 1994].

[20] Figure 4 compares the LWP_V and LWP_T values for all warm overcast nonprecipitating clouds observed by TRMM during July 1998. The correlation coefficient is 0.68, much higher than the 99% significance level. The root mean square (rms) difference between these data is 0.028 mm and the mean difference is −0.005 mm or ~6%. The larger mean value from VIRS may arise for several reasons including possible overestimation of optical depth or effective droplet radius r_e. Cloud optical depth may be overestimated at high solar zenith angles because of three-dimensional effects that occur in nature but are not taken into account in the plane-parallel retrieval model. The derived value of r_e often corresponds to the top

portion of the cloud and may overestimate r_e integrated over the entire cloud depth. Use of the freezing temperature as a threshold does not ensure that all ice cloud contamination is eliminated from the VIRS retrievals. Optically thin ice clouds over warm water clouds can be mistaken as liquid water clouds with larger than normal droplet sizes and with a mean value of $Tc > 273$ K resulting in an overestimate of LWP. Thus residual ice cloud contamination could be responsible for the small overestimate of mean LWP_V relative to mean LWP_T.

[21] The scatter in Figure 4 suggests that LWP_V exceeds LWP_T more often for small LWP_T values than for larger values and vice versa. This apparent behavior of the LWP differences with LWP_T may be due to several factors. The parameterization used for VIRS Edition 1 to derive optical depth (OD) from the visible reflectance field slightly overestimates OD for optically thin clouds and underestimates OD for thick clouds. Additionally, the small amount of atmospheric water vapor absorption in the visible channel was also not taken into account in the Edition-1 retrievals. This effect, which would artificially decrease OD is more important for the large ODs because small changes in reflectance result in greater changes in OD for large OD and would cause the LWP_V to be smaller than LWP_T at the larger values of LWP_T. These parameterization and absorption effects, eliminated in the upcoming VIRS Edition 2 product [Minnis et al., 2002], should have little impact on the conclusions of this study. Another possible reason for the large LWP_T relative to LWP_V may be due to large (>16 μm) effective cloud water particles or drizzle cases [Lin et al., 1998b]. In these cases, the cloud particle sizes are relatively small compared with the SSM/I wavelengths and can't produce significant microwave scattering. Thus there is little effect on current microwave LWP retrieval technique. However, for VIRS retrievals, the effective particle sizes are underestimated due to signifi-
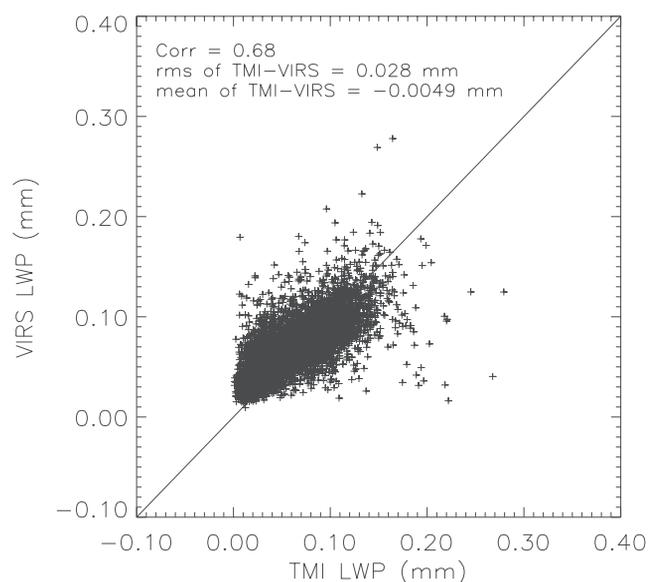
Corr = 0.68
rms of TMI−VIRS = 0.028 mm
mean of TMI−VIRS = −0.0049 mm

Figure 4. Comparison of LWP_T and LWP_V for 1° × 1° grid boxes for all warm overcast nonprecipitating clouds during July 1998.
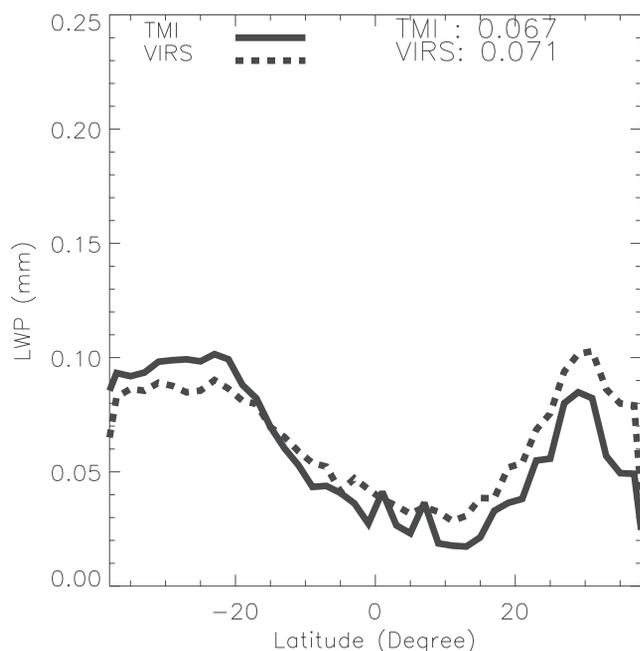
Figure 5. Zonal mean LWP_T and LWP_V values for warm overcast nonprecipitating clouds for July 1998.

cant differences in cloud particle size between upper parts and lower parts of the clouds. The underestimation results a biased low LWP_V, and causes $LWP_T > LWP_V$. Because drizzling clouds usually hold considerable amounts of water, this effect is more obvious for large LWP cases as shown in the figure. Other factors, such as calibration uncertainties for TMI cloudy pixels and/or the errors produced by the differences in the TMI sampling (or beam-filling) patterns for the various wavelengths (more details of the uncertainties of LWP_T retrievals are discussed in 6.1), may also generate larger LWP_T values.

4.3. Zonal Mean WP_V and LWP_T for Warm and Cold Nonprecipitating Clouds

[22] Further temporal and spatial comparisons of the collocated LWP_V and LWP_T for warm, nonprecipitating overcast clouds were performed to cross validate the near-global (from 38°N to 38°S) LWP distribution for different seasons. The zonal mean LWP_V and LWP_T results for July 1998 (Figure 5) agree well over most places. VIRS underestimates LWP over the southern hemisphere from 45°S to 20°S relative to the TMI. Larger differences are found in the regions north of 30°N where considerably fewer samples were obtained from *TRMM*. The mean difference between the results varies with month ranging from 0.004 mm in August to 0.015 mm in January (not shown). The average difference for all 8 months is less than 0.01 mm, similar to those found in the scatterplot (Figure 4) and to the LWP bias error from the simulation study [*Lin et al.*, 1998a].

[23] The reasons for differences in the zonal LWP means may partially result from the previously mentioned error sources. Additionally, there may be some water-vapor-dependent biases that result from the uncertainties in the

absorption coefficients used in the MWRTM. A closer examination of the results will be addressed in a future study. For regions dominated by stratus and stratocumulus clouds with no indication of contaminating cirrus clouds the LWP_V and LWP_T values are more highly correlated. The mean difference, $LWP_V - LWP_T$, in such regions can be as low as 0.005 mm with a standard deviation of 0.004 mm (not shown). Further discussion can be found in *Ho et al.* [2001]. Thus it is likely that much of the bias in Figure 5 north of 30°N may be due to mostly some residual cirrus contamination.

[24] The LWP_T values (0.042 ± 0.041 mm) for cold ($Tc <$ 273 K), nonprecipitating overcast clouds are 0.090-mm smaller than WP_V (0.132 ± 0.133mm). Large LWP_T and WP differences for cold nonprecipitating clouds were also found by *Lin and Rossow* [1994, 1996], who applied a technique similar to the MVI to SSM/I and ISCCP data. They found that, as a fraction of the ISCCP total water path, the mean SSM/I-estimated LWP varied from 22% in the Tropics up to 55% in the southern midlatitudes. LWP_T is between 25 and 30% of the magnitude of WP_V (see below), a value closer to the tropical end of the range from *Lin and Rossow* [1996]. The results from the present and previous studies are fairly consistent given the differences in time and data sets. This consistency in the mean values of the LWP/WP ratios belies the expected differences in instantaneous values. The tight match between the imager and microwave data obtained here significantly reduces spatial and temporal uncertainties. Furthermore, the explicit retrieval of OD and particle sizes for both water and ice clouds applied to the VIRS measurements [*Minnis et al.*, 1995] yields a different measure of WP_V than would have been derived using the same approach as the ISCCP. As pointed out by *Lin and Rossow* [1996], the large difference between LWP_T and WP_V is mainly caused by cloud IWP. In most of these cases, ice phase is detected and interpreted in the VIRS retrievals. By comparing with LWP_T, it is possible to attribute almost 25 to 30% of the magnitude of WP_V in these cases to liquid water beneath the upper-layer clouds. Thus the assumption that the cloud is entirely ice used in the IWP retrieval introduces some errors in the WP_V estimations. However, the error may not be too significant on average, since LWP is only about a quarter of the apparent water amount. Also, liquid water clouds occur beneath the ice clouds and contribute less to the VIRS-observed radiances compared with the ice cloud at the top layer.

[25] The zonal means of LWP_T and WP_V for cold overcast nonprecipitating clouds for January, April and July are shown in Figures 6a, 6b, and 6c, respectively. IWP_{TV} is estimated to be equal to the difference between WP_V and LWP_T. Figure 7 shows IWP_{TV} estimated from the differences for the 3 months, along with the VIRS-estimated ice water path IWP_V for all TMI FOVs containing only ice-phase VIRS pixels [*Minnis et al.*, 1999] for the same time periods with $LWP_T < 0.1$ mm. The latter threshold is used to minimize the impact of LWP on the IWP retrieval. To ensure a sufficient number of samples, cloudy pixels with $LWP_T < 0.1$ mm are used instead of using only cloud pixels having $LWP_T < 0.04$ mm. The average IWP_V from pixels with $LWP_T < 0.1$ mm is only about 3% larger than that from cloud pixels with $LWP_T < 0.04$ mm. The slightly greater average IWP_V compared to the combined IWP_{TV} means can
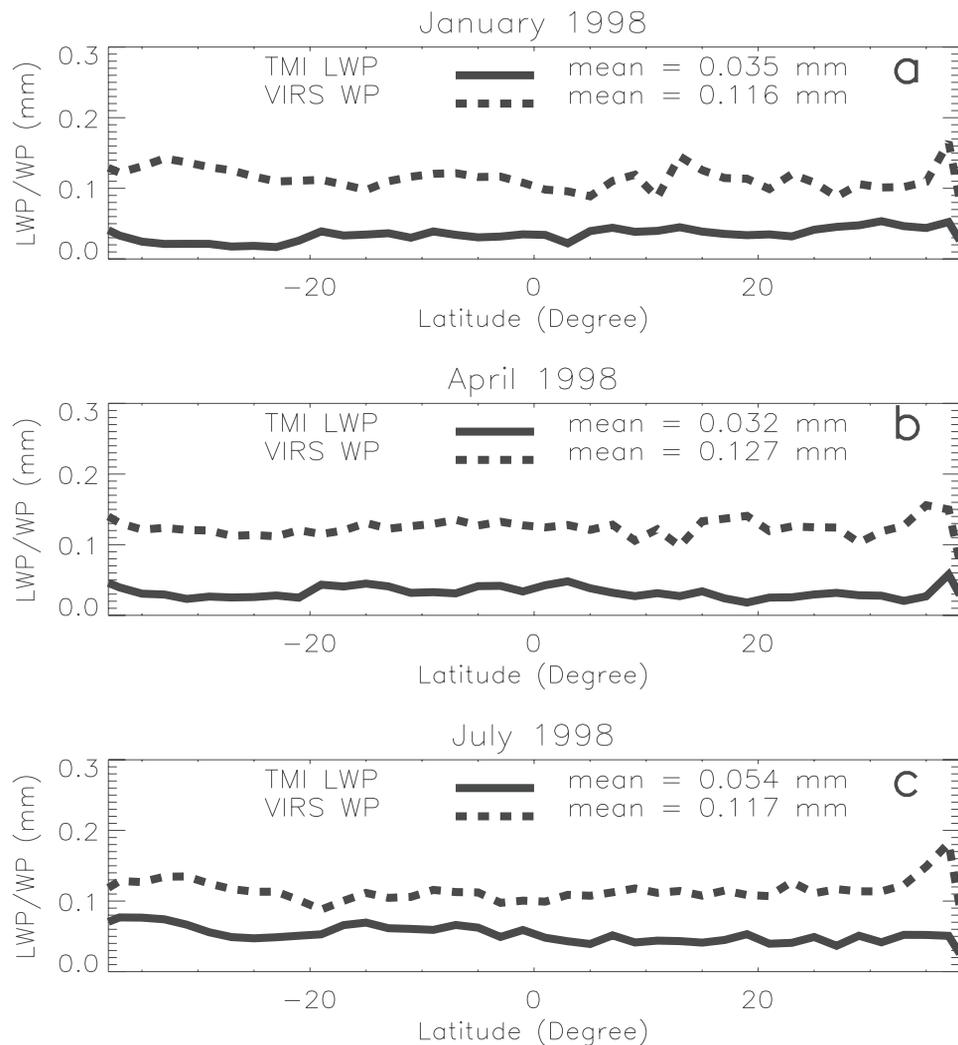
Figure 6. Zonal mean for LWP_T and WP_V for cold overcast nonprecipitating clouds for (a) January (b) April and (c) July 1998.

possibly be due to some small residual amount of lower-level liquid-water contamination because of the nonzero LWP_T threshold, to the differences between the definitions of LWP_V and IWP_V discussed below, or to slight differences in the conditions generating the ice clouds in otherwise clear skies and in the presence of lower-level clouds. The consistent IWP retrievals derived from two independent data sets lend confidence to the IWP values and demonstrate the efficiency of each retrieval technique. The similarities in the two quantities also suggest, however, that the cloud formation conditions are much the same regardless of the lower-level cloud situation in the absence of precipitation. Seasonal variations of water path minima (and ice water path minima) due to the shifting of the general circulation can also be seen in Figure 6. LWP_T under the cold clouds is less variable zonally than LWP_T for warm clouds (Figure 5) especially during January. The maximum in LWP_T occurs near the ITCZ in April and south of 20°S during July. When water clouds occur below the ice clouds, and the VIRS retrieval interprets the systems as single-layered ice clouds, the particle sizes for the water layer are overestimated, along with some underestimation in optical depth. It has not been determined if these effects compensate each other resulting in an unbiased estimate of WP_V or if they cause a bias in WP_V.

5. Single-Layered and Overlapped Clouds

5.1. Top and Base Heights of Single Layer Water Cloud

[26] Warm water clouds ($Tc > 273$ K) comprise about 40 to 50% of the total cloud cover in the *TRMM* domain. According to *Charlock et al.* [1994], cloud thickness and base height statistics can be used to more accurately compute the longwave radiative divergence at the surface and within the atmosphere. On the basis of the previous estimates of cloud layer thickness for low (~700 m), middle (~1200 m) and high (~2500 m) clouds, a set of thresholds for tropical and middle latitudes was established to determine the occurrence of overlapped clouds (in section 3). The warm liquid-water clouds ($Tc > 273$ K) not classified as overlapped clouds are assumed to be single-layered. The single-layer cloud top (equation (4)) and base heights (equation (5)) and cloud thickness (equa-
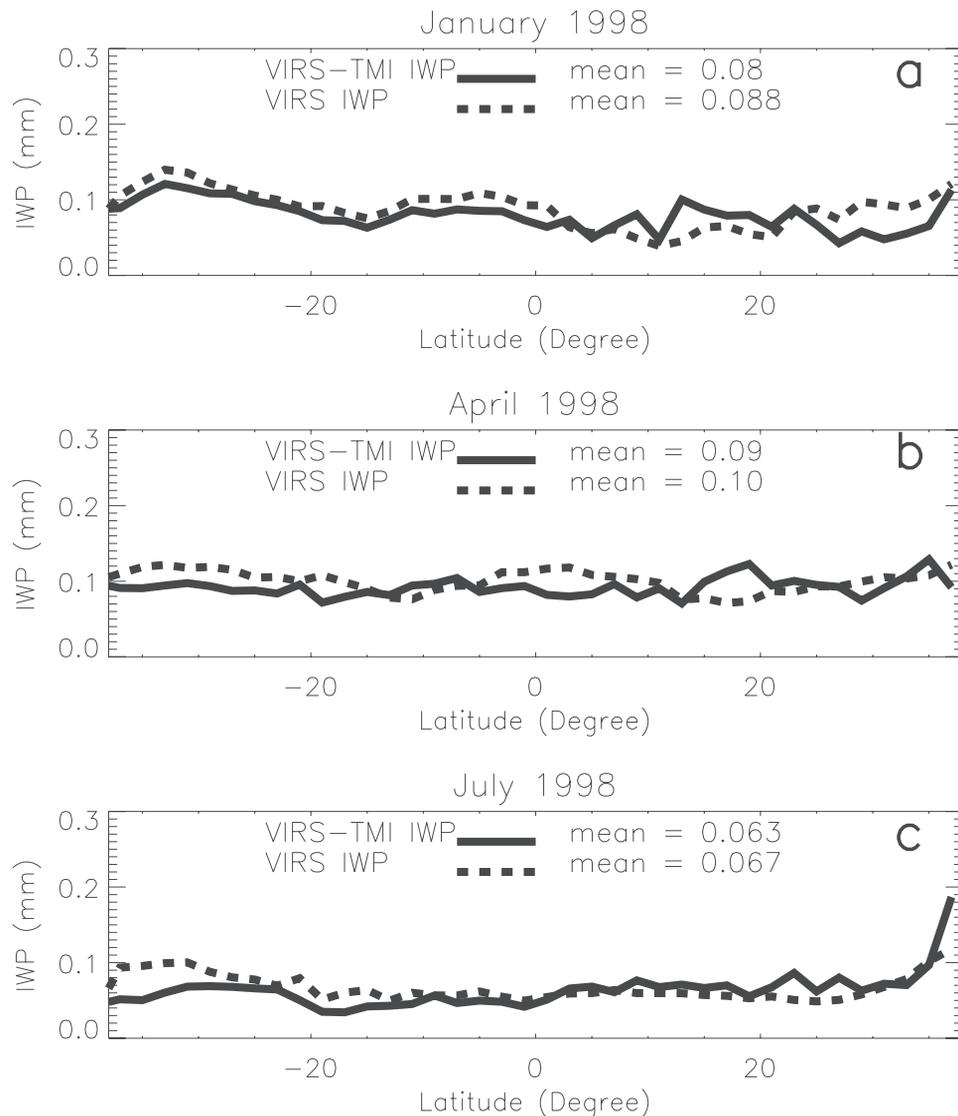
Figure 7. Same as Figure 6, except for IWP ($=WP_V - LWP_T$) along with the VIRS estimated IWP for (a) January (b) April and (c) July 1998.

tion (3)) were computed using Tc, Tw, SST, and a climatological lapse rate ($\Gamma = -6.5$ K/km for tropical atmospheres and $\Gamma = -7.1$ K/km for midlatitude regions).

[27] Warm nonprecipitating clouds with $LWP_T > 0.04$ mm and $\Delta Twc < 8$ K for low clouds and $\Delta Twc < 10$ K for midlevel clouds are classified as warm single-layer clouds. With the assumption that Tc corresponds closely to cloud top while Tw is more representative of the cloud center, cloud top and base heights were estimated from the MVI retrievals. There were only 8 months of TMI and VIRS Edition-1 data available for the current analyses. Data from January are used here to represent the climate during the boreal winter. The latitudinal variations of mean cloud top height, cloud base height, and cloud thickness for January are shown in Figures 8a and 8c for single-layer low and midlevel clouds, respectively. The low cloud top and base heights are around 1.5 and 0.7 km, respectively, with minimal zonal variation. The mean cloud thickness is also nearly invariant near an average of 800 m. Midlevel cloud-top heights exhibit a wider range than those for low clouds.

The mid-level clouds occurring over the ITCZ are thicker and higher than elsewhere. The distribution of mean cloud-base altitudes mimics the cloud-top altitude variation. The midlevel cloud thickness peaks between 0° and 20°S at ∼1300 m.

[28] Figures 8b and 8d depict the zonal variations of mean July cloud top and base height, and cloud thickness for low and midlevel clouds, respectively. A slight gradient in low-cloud top height and thickness is apparent in Figure 8b with an increase in both quantities from north to south. The appearance of this gradient results from a drop in the mean low-cloud height from 1500 m to ∼1000 m at 25°N. The peak mean midlevel cloud altitude follows the January-to-July ITCZ movement from south to north (Figure 8d). During both months, the maximum mean top altitude is ∼3.8 km for midlevel clouds. The midlevel cloud thickness has a broad maximum of ∼2000 m between 5°S and 20°N. The low-cloud-base altitudes are, on average, very close to the corresponding top heights of the low clouds studied by *Poore et al.* [1995]. The low-cloud thicknesses in Figure 8a
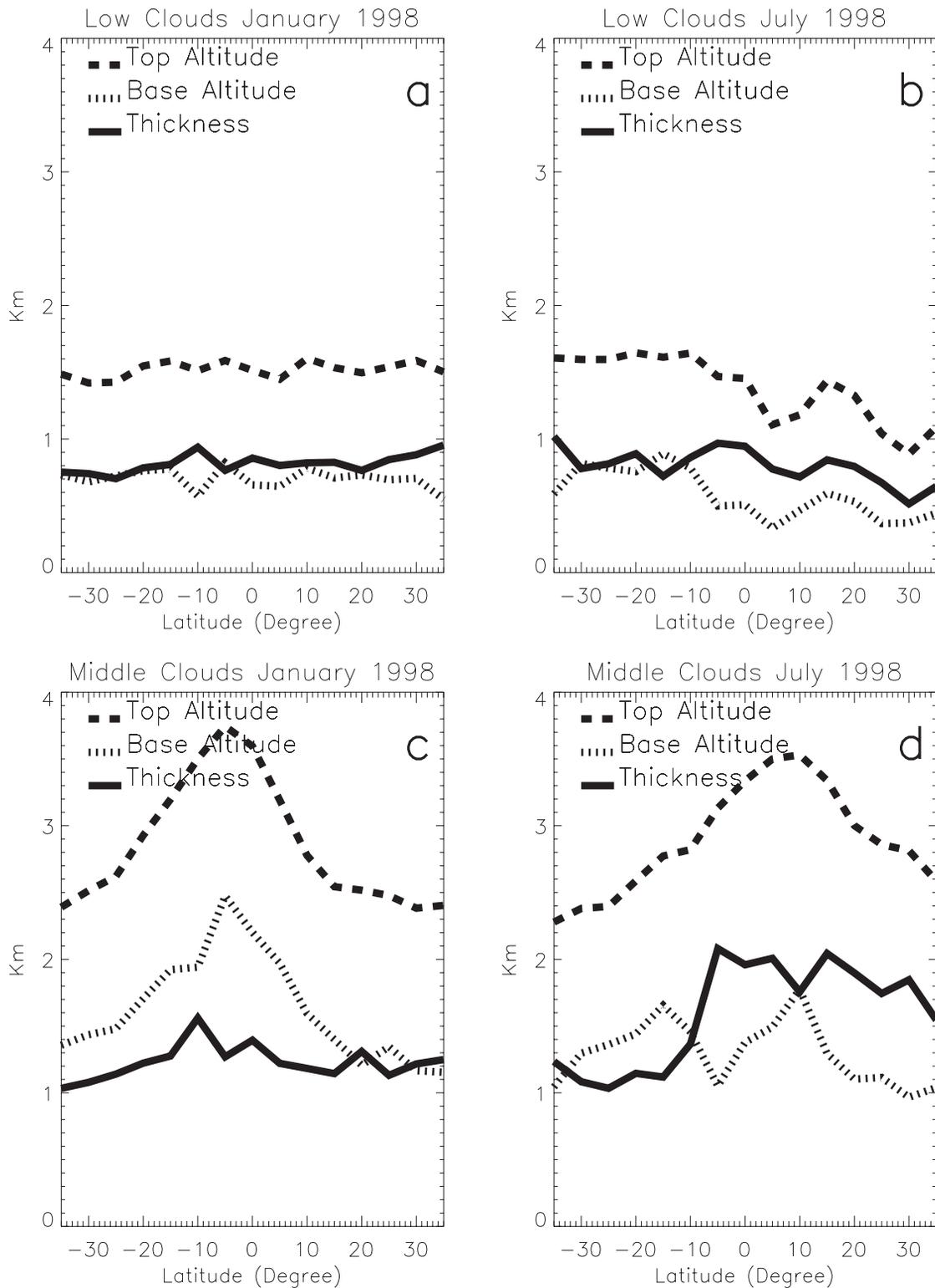
Figure 8. The latitudinal variations of cloud top height, cloud base height, and cloud thickness for January 1998 for (a) low clouds and (c) middle clouds. The latitudinal variations of cloud top height, cloud base height, and cloud thickness for July 1998 for (b) low clouds and (d) middle clouds.

(~800 m) and 8b (~1000 m) are within the reasonable ranges between the 799 and 1263 m reported by *Poore et al.* [1995] over northern ocean regions for stratus and cumulus cloud types. The small differences between the

mean values can arise for a variety of reasons including the sparse sampling in the *Poore et al.* [1995] data set, uncertainties in converting relative humidity profiles to cloud locations, differences in low-cloud definitions, and uncer-

Table 1. The Summary of Cloud Statistics (in %) for All Eight Months[a]

	$f_w(= W/N_T)$	$f_c(= C/N_T)$	f_{low}	f_{mid}	f_{high}	f_{olow}	f_{omid}	f_{ohigh}
Global	43.4	56.6	26.8	30.5	24.2	3.97	15.58	37.6
Tropics	41.2	58.8	21.3	25.4	32.7	3.6	11.25	32.8
Northern Hemisphere	43.7	56.3	32.3	35.4	18.1	3.3	19.1	40.59
Southern Hemisphere	45.2	54.8	35.4	30.4	17.6	5.0	16.4	39.43

[a]W means warm cloud pixels, C means cold cloud pixels, N_T is total cloud pixels (including overcast and cloudy). f_{low}, f_{mid} and f_{high} are the percentages of low, middle and high cloud of the total pixels (clear + cloud), respectively. f_{olow}, f_{omid}, and f_{ohigh} are the frequency (%) of the occurrence of cloud exist below overcast low, middle and high cloud pixels, respectively.

tainties in the correspondence between Tw and relative altitude within the cloud. This last uncertainty is probably the main cause for the difference in cloud base height since the long-term observations of St and Cu base heights over ocean [*Warren et al.*, 1988] are generally around 500 m compared to the 700 m (Figure 8a) and 600 m (Figure 8b), respectively. However, the small variations in cloud base height in Figures 8a and 8b are consistent with the small range in St base height from *Warren et al.* [1988]. If an uniform lapse rate $\Gamma = -7.1$ K/km was used over tropical region (instead of using $\Gamma = -6.5$ K/km), the shape of Figures 8a, 8b, 8c and 8d do not change significantly (the changes are less than 10% from the original results in tropical regions), and the results are still very close to corresponding low- cloud results derived from the combination of surface and upper-air observations [*Poore et al.*, 1995].

5.2. Global and Regional Variations of Overlapped Clouds

[29] The frequencies of different cloud types were computed from the matched VIRS and TMI cloud products for all 8 months. The frequency of warm clouds f_w is the fraction of all warm TMI cloud pixels relative to the total number N_T of TMI cloud pixels; f_{low} is equal to the fraction of all low-cloud pixels divided by all TMI cloud pixels. The frequencies of different types of clouds for global (37°N−37°S), tropics, Northern Hemispheric midlatitudes, and Southern Hemispheric midlatitudes are summarized in Table 1. The occurrences of the multilayered systems under overcast conditions are also listed (i.e., the f_{olow}, f_{omid} and f_{ohigh} in Table 1 denote the frequency (%) of the occurrence of cloud below the overcast low, middle and high TMI cloud pixels, respectively). In general, warm cloud pixels ($Tc > 273.1$ K) occupy 40% of the total cloud (cloudy + overcast) pixels. The corresponding low, middle and high cloud fractions relative to the total TMI pixels vary with season and climatological region, and the total cloud fraction is around 80% (i.e., 80% TMI pixels contain clouds), which is consistent with global cloud frequency obtain from HIRS [*Wylie et al.*, 1994] where the HIRS footprint is comparable to that of TMI. There is no significant difference in the total cloud frequency for different climatological regions. The frequency of high clouds in the Tropics (f_{high}; the percentage of the high cloud (cloudy + overcast) of the total tropical TMI cloud pixels) is greater than those in the midlatitudes, and the tropical low and middle cloud frequencies are less than those in the midlatitudes. *Hahn et al.* [1982, 1984] and *Warren et al.* [1985] found that the maximum occurrence of cirrus clouds over oceans (~35%) is found near the mean latitudes of the ITCZ, and that the St and Sc

frequencies tend to increase toward the poles (~28% near the equator and 34% at 30° N), whereas the frequency of cumulus tends to decreases (48% at tropics and 30% at 30°N).

[30] The frequency of precipitating cloud is around 8.8% of all pixels, while overcast clouds comprise 13% of total cloud pixels. For low clouds, the co-occurrences of multilayered clouds are less than 4% for all regions. Although boundary layer clouds occasionally overlap with other water clouds below, as described in Figures 2a and 2b, the ΔTwc is generally so small that most of the overlapped clouds cannot be separated by the MVI technique. The overall frequencies of middle and high overlapped clouds are about 16% and 38%, respectively. The overlapped cloud frequency of high overcast clouds in the Tropics is tightly linked to the extensive cirrus sheets over the tropics. Ground observations [*Hahn et al.*, 1982] reveal that tropical cirrus clouds often overlap cumulus and cumulonimbus underneath. The high cloud co-occurrence in the Tropics from the TMI-VIRS analyses is about 4% lower than estimated from rawinsondes [*Wang et al.*, 2000]. The difference is probably due to the elimination of TMI pixels with small water amount (LWP < 0.04 mm) and the sparse sampling from the balloons. Thin cirrus or water clouds (with estimated optical depth < 6 and LWP < 0.04 mm) above lower level water clouds may be excluded from our estimations.

5.3. Geographical and Seasonal Distributions of Overlapped Clouds

[31] The 1° gridded occurrences of high, middle and low clouds for July are shown in Figure 9. (Note, for this and other plate plots, because of lacking color scale, white regions represent 0% cloud cover.) High clouds (Figure 9a) occurred most frequently during July along the ITCZ and over regions with large SSTs (10°S to 30°N), especially over the Indian Ocean (20% to 80%) and Indonesia (40% to 80%). High clouds were less frequent over the descending regions of the Hadley and Walker cells where middle and low clouds were found more frequently (Figures 9c and 9e). The 20 to 30% frequency of high clouds over the midlatitudes around 30°S near the east coasts of Australia and South America may be associated with frontal activity during the winter.

[32] Middle clouds occur more frequently over southern hemisphere in this season (Figure 9c). These altostratus and altocumulus are mainly produced by winter cyclones. Very few middle clouds are found in the northeast Atlantic Ocean, the east Pacific Ocean near tropics, the west coast of the South America and the west coast of the South Africa from 15°S to 0° where persistent low clouds dominated (Figure 9e).
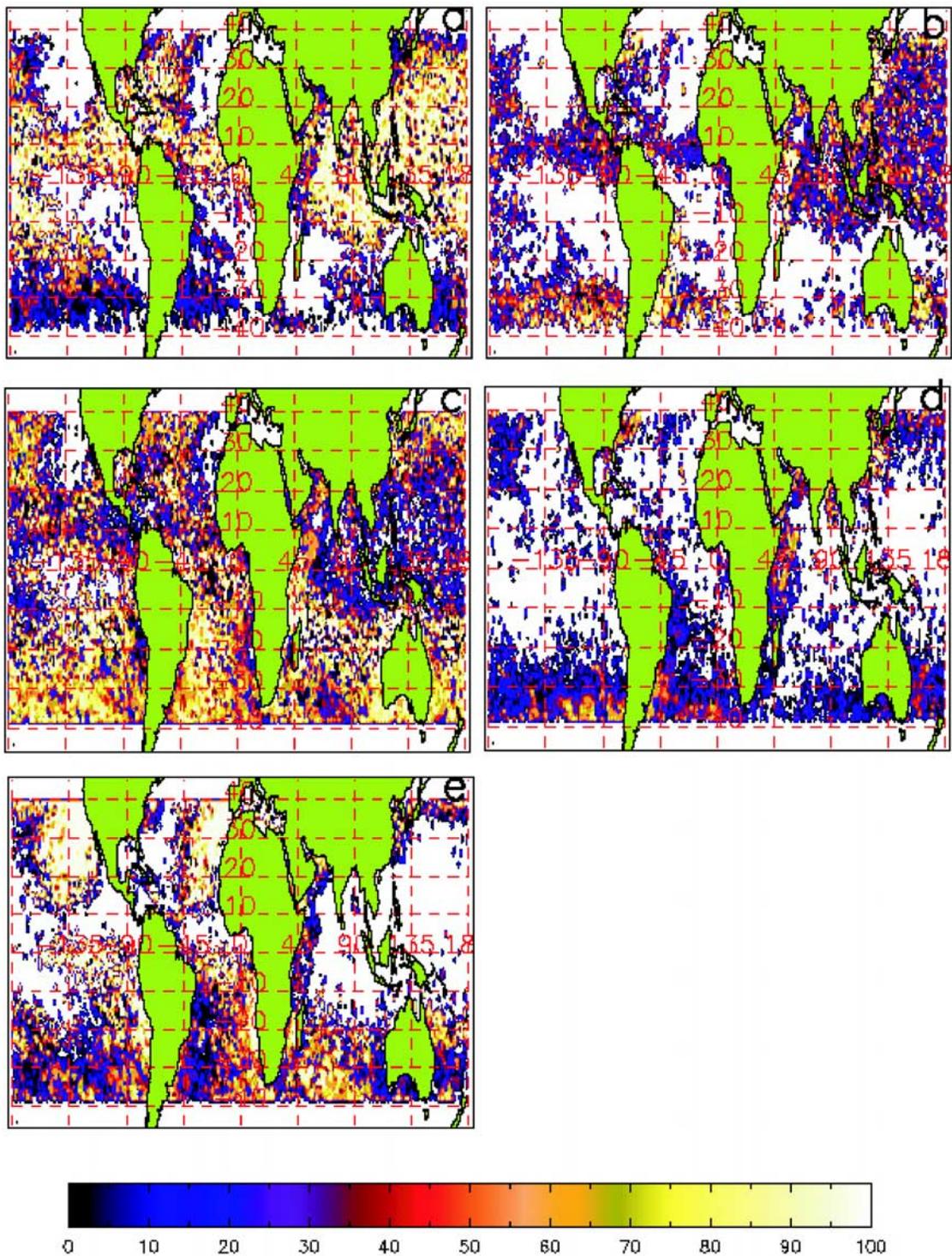
Figure 9. 1° averaged (a) high, (c) middle and (e) low overcast nonprecipitating cloud occurrences (in %) for July and corresponding overlapping cloud frequencies for (b) high clouds and (d) middle clouds.

[33] The 1°-grid-averaged overlapped high clouds for July are shown in Figure 9b. It can be seen that the geographical distributions of high overlapped clouds are correlated with high cloud distributions. As expected, much fewer high overlapped clouds are detected over sub-tropical subsidence areas, and high-level clouds co-occurring with lower clouds occupied a larger area in the northern hemisphere (summer regions) than those in the southern hemisphere (winter regions). The result that the cloud water temperatures for those lower level clouds beneath high clouds in tropical and northern hemisphere (summer regions) are between 233 K and 270 K is consistent with the ground-based observations from *Hahn et al.* [1982]. Although high clouds only occur 20 to 30% of the time off the east coast of South America,
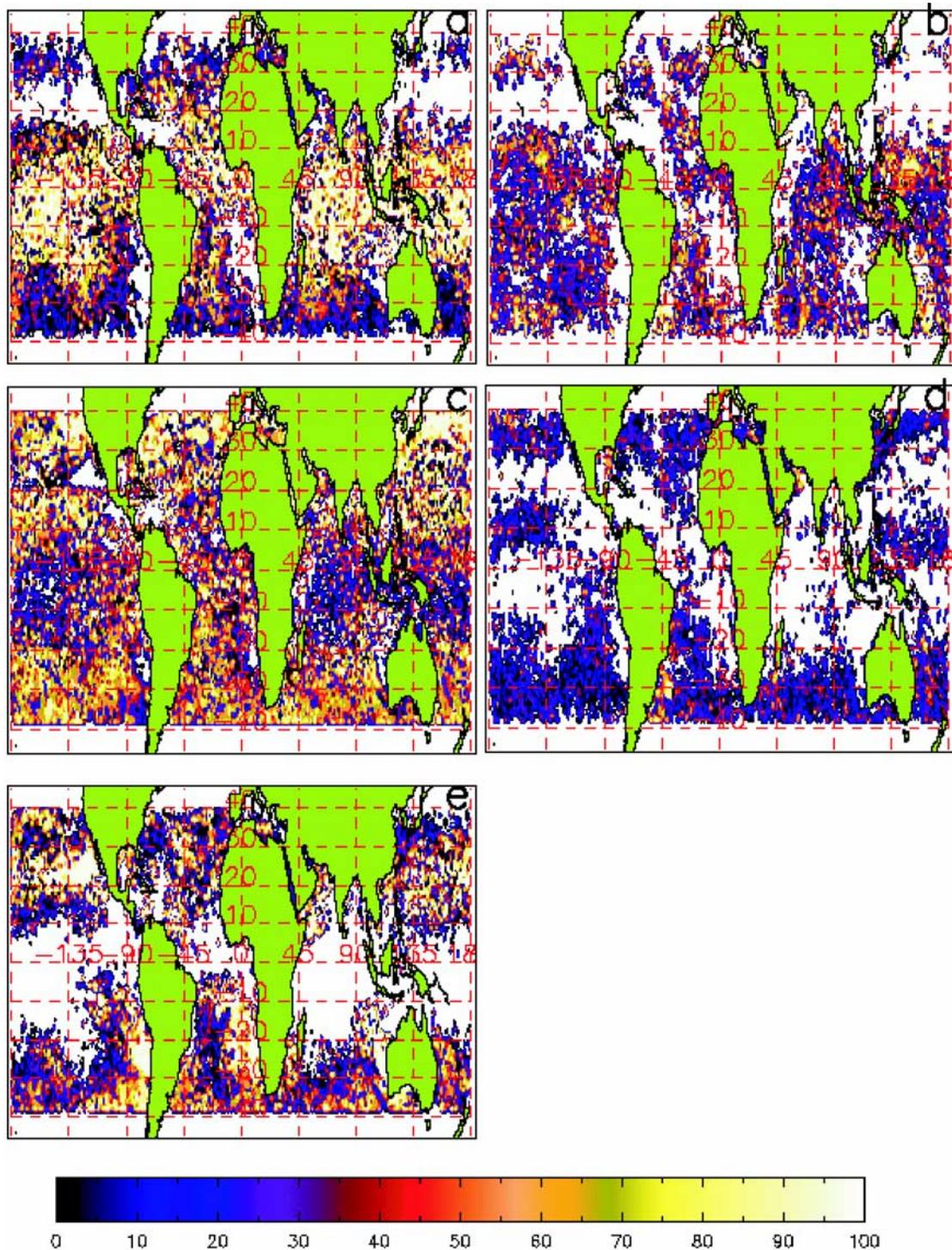
Figure 10. 1° averaged (a) high, (c) middle and (e) low overcast nonprecipitating cloud occurrences (in %) for January and corresponding overlapping cloud frequencies for (b) high clouds and (d) middle clouds.

Australia and the east coast of South Africa (10°S to 10°N) during the winter, warm water clouds ($Tw > 273$ K and $LWP_T > 0.04$ mm) beneath cirrus clouds are frequently (50–60%) detected by TMI measurements in these regions. The distributions of overlapped middle clouds are very similar to those for middle clouds (Figure 9d). The overlapped middle clouds often occur more over sub-tropical subsidence areas.

In addition, most of those middle clouds are altostratus and altocumulus and the low clouds beneath the middle clouds are mainly St or Sc.

[34] To illustrate the seasonal variations of overlapped clouds, the geographical distributions of the high, middle and low cloud and their overlapping frequencies for January are shown in Figure 10. Compared with Figure 9,

the maximum high clouds and overlapped high and mid-level clouds shifted from 0°–20°N to 10°N–20°S. Most overlapped clouds occur in south hemisphere (summer) regions.

[35] The zonal averaged overlapping cloud frequencies for January and July 1998 are shown in Figures 11a and 11b, respectively. The maximum co-occurrence of high clouds coincides with the ITCZ during January but is relocated to 35°S and 35°N during July with secondary maxima in the Tropics. The latitudinal variation of water cloud cover is less than 10% for different seasons (not shown). Overlapping of high clouds occurs more often over tropical regions, gradually decrease in the sub-tropics. The greater overlapping cloud frequency in the winter hemisphere around 30°S (Figure 11b) may be due to the occurrence of stratus and stratocumulus beneath cirrus clouds generated mainly from frontal activities. The reason that overlapping cloud frequencies in these regions from surface observations [*Warren et al.*, 1985] are much less than those from MVI may be because surface observers have difficulty identifying altostratus/altocumulus and cirrus when low clouds are present. Additionally, the sampling from surface observations is sparsest in the Southern Hemisphere, where clouds over vast areas are unobserved.

[36] The monthly variations of mean high, middle, and low cloud overlapping frequencies are shown in Figure 12 for January through August 1998. No significant variations of overlapped clouds are found except for the peak in midlevel overlapping clouds during July. The mean co-
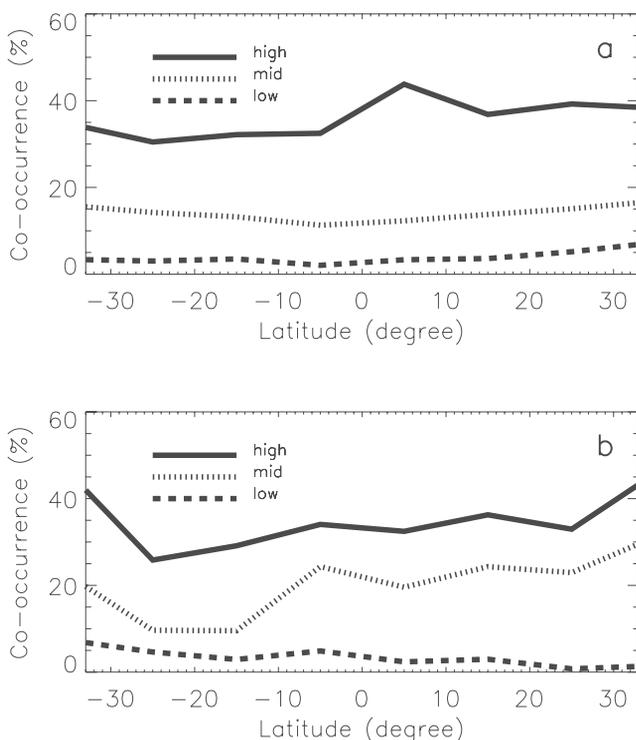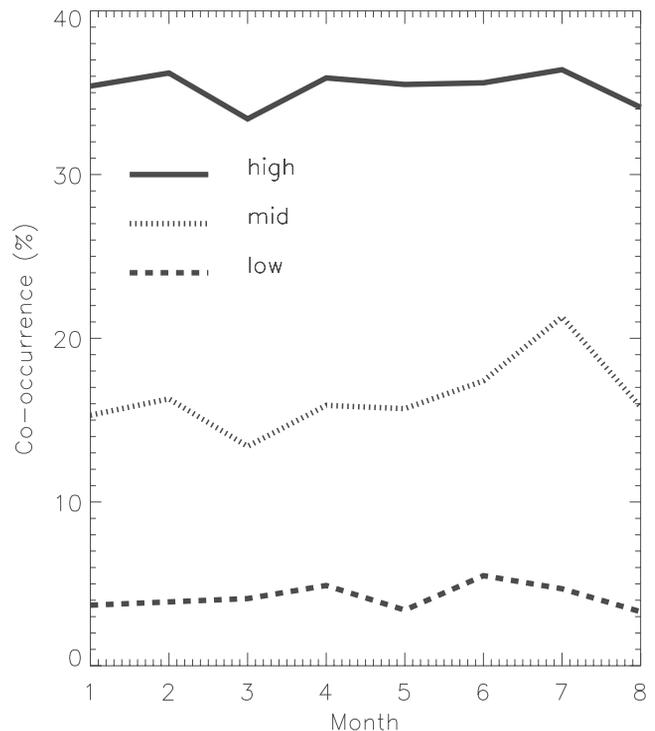

Figure 12. Monthly variations of the overlapping cloud frequencies for overcast nonprecipitating high, middle and low clouds for regions.

occurrence for high, middle and low clouds are 37, 16, and 4%, respectively.

6. Discussion and Conclusions

6.1. LWP, Tw, and IWP Retrievals

[37] The uncertainties in LWP_T and Tw are primarily due to errors in the retrieval inputs (*SST*, *WS*, and *CWV* and TMI instrument noise and the calibration uncertainties) and the errors produced by the differences in the TMI sampling (or beam-filling) patterns for the various wavelengths. The bias between the *CWV* retrievals and the results retrieved from the scheme adapted from *Schluessel and Emery* [1990] for TMI is about 4.2 kg/m². The root mean square error for the *Schluessel and Emery* [1990] technique is about 5.31 kg/m² compared to radiosonde data. The *Tb* error resulting from the individual uncertainties in *SST*, *WS* and *CWV* are not discussed here. However, the combined uncertainties of the input *SST*, *WS* and *CWV* to the LWP retrievals are about 0.04 mm (Figure 3). The bias-corrected Tb_{85V} and Tb_{37H} values for clear sky are very close to the TMI measurements. The root mean square error between the bias-corrected Tb_{85V} and the TMI-measured Tb_{85V} is 0.09 K, and that for Tb_{37H} is 0.24 K (not shown). The errors caused by sampling (or beam-filling) differences between the 37 and 85-GHz channels are difficult to evaluate. Generally, TMI lacks the secondary scans, such as the B-scans taken by the SSM/I, between its primary scans, leaving considerable gaps for the highest frequency channels. Thus there are some sampling differences between the measurements at 37 and 85 GHz, especially when the clouds are broken. Because many clouds, especially those in overcast condi-

Figure 11. Zonal averaged overlapping cloud frequencies for high, middle and low overcast nonprecipitating clouds for (a) January and (b) July 1998.

tions, are continuous over 45 km or more [*Tian and Curry*, 1989], and the present analysis is mostly concentrated on overcast cases, the errors are minimized. The averaging of the TMI pixels on the 1° grid reduces the errors. The correlation coefficients between the collocated VIRS cloud cover in 85-GHz FOVs and that in the 37-GHz FOVs are more than 0.9 under overcast conditions and the mean respective cloud amounts are 98.8% and 99.4%. The overall instantaneous LWP_T uncertainty is ±0.04 mm (Figure 3). For 1° gridded data, the Tw uncertainty is about 3 K.

[38] The overall 6% difference is consistent with the comparisons of LWP derived from surface MW radiometers and from VIRS and the Geostationary Operational Environmental Satellite (GOES) over the Atmospheric Radiation Measurement (ARM) site in Oklahoma. *Dong et al.* [2002] found that, on average, *LWP* derived from GOES with the same algorithm used for the VIRS analyses was 4% greater than the surface-based LWP for 71 matched St cases during March 2000. The mean LWP_V from 25 cases of VIRS data was 14% greater than the average from the matched surface microwave retrievals for stratus clouds observed between January and July 1998 over the ARM site. The differences are caused by the uncertainties in the derived effective radii and optical depths. The results presented here rely on preliminary (Edition 1) retrievals from the CERES cloud algorithms. Several changes that have been introduced in the CERES algorithms since the current analyses were performed may slightly change LWP_V. The new CERES results [*Minnis et al.*, 2002], including additional months, will be examined in future studies.

[39] Both IWP and LWP are critical for improving model simulations of weather and climate. The uncertainty in the IWP retrieval primarily arises from the LWP_T and WP_V retrievals. The good agreement between LWP_T and LWP_V for overcast nonprecipitating warm clouds should lend confidence to the LWP_T for cold clouds. However, quantitative analysis of the uncertainties in IWP is not yet available. In the future, the MVI-derived IWP should be validated using observational data from field campaigns.

6.2. Overlapped Cloud Retrievals and Cloud Vertical Distribution

[40] The threshold used here may cause some uncertainties in overlapping cloud frequency. Because the ΔTwc distribution for middle clouds is narrower than that for high clouds, the resulting middle cloud overlapping frequency may be more sensitive to the thresholds of cloud thickness than that for high clouds. The broader ΔTwc distribution for high clouds (Figure 2f) makes the high cloud overlapping frequency less sensitive to the threshold. There could be less than a 4% difference in the overlapping frequency of high clouds by using the high cloud thickness of ~2500 m estimated by *Wang and Rossow* [1995] in one case and the 1700-m thickness derived from *London* [1957] in the other. Thus even with the conservative threshold of $\Delta Twc > 15K$, the overlapping frequency is only 4% less than *Wang and Rossow* [1995] as discussed before.

[41] In summary, the results shown here provide additional confidence in the retrievals of LWP using cloud optical depth and effective radius from VIS and IR measurements over both land and ocean and to the potential for retrieving IWP and LWP simultaneously in overlapped conditions using the

MVI technique over ocean. Thus it is possible to monitor cloud water path in nearly all-daytime conditions using combinations of satellite sensors. By minimizing the errors in each retrieval technique and applying them together on satellites like *TRMM*, it will be possible to provide the water path data needed to constrain and validate climate model calculations of clouds and radiation. The derived geographical and seasonal variations of overlapping cloud frequency and cloud thickness provide unique cloud vertical distribution information and will be useful for surface radiation balance and hydrological cycle studies.

Notation

ARM	Atmospheric Radiation Measurement
As	altostratus
ASTEX	Atlantic Stratocumulus Transition Experiment
CERES	Clouds and Earth's Radiant Energy System
CWV	column water vapor
f_{low}	frequency of low clouds
f_{olow}	the occurrence of cloud below the overcast low TMI cloud pixels
f_{omid}	the occurrence of cloud below the overcast middle TMI cloud pixels
f_{ohigh}	the occurrence of cloud below the overcast high TMI cloud pixels
f_w	frequency of warm clouds
FOV	field of view
GOES	Geostationary Operational Environmental Satellite
H	horizontal polarization
H_{CLD}	the single-layered water cloud thickness in km,
IR	infrared
ISCCP	International Satellite Cloud Climatology Project
ITCZ	Intertropical Pacific Convergence Zones
IWP	ice water path
IWP_{TV}	$WP_V - LWP_T$.
LUT	lookup table
LWP_T	TMI liquid water path
LWP	liquid water path
LWP_V	VIRS liquid water path
IWP_V	VIRS ice water path
MVI	microwave, visible and infrared
MW	microwave
MWRTM	microwave radiation transfer model
N_T	total number of TMI cloud pixels
OD	optical depth
r_e	droplet radius
rms	root mean square
Sc	stratocumulus
SIR	solar infrared,
SSM/I	Special Sensor Microwave/Imager
SST	sea surface temperature
St	stratus
SPCZ	Southern Pacific Convergence Zones
Tb	microwave brightness temperature
TMI	TRMM Microwave Imager
TRMM	Tropical Rainfall Measuring Mission
Tw	cloud water temperature
Tc	cloud-top temperature
V	vertical polarization

VIRS   Visible and Infrared Scanner
VIS   visible
WP, WP_V total water path, VIRS total water path
WS near-surface wind speed
z_T cloud top height
z_B cloud base height
Γ atmosphere lapse rate
ΔTwc $=Tw - Tc$

References

Baum, B. A., and J. D. Spinhirne, Remote sensing of cloud properties using MODIS airborne simulator imagery using SUCCESS, 3: Cloud overlap, *J. Geophys. Res.*, *105*, 11,793–11,801, 2000.

Charlock, T., F. Rose, T. Alberta, G. L. Smith, D. Rutan, N. Manalo-Smith, P. Minnis, and B. Wielicki, Cloud profiling radar requirements: Perspective from retrievals of the surface and atmospheric radiation budget and studies of atmospheric energetics, utility and feasibility of a cloud profiling radar, *WCRP-84, JGPO Publ. Ser 10*, pp. B10–B21, World Clim. Res. Program, Geneva, 1994.

Dong, X., P. Minnis, G. G. Mace, W. L. Smith Jr., M. Poellot, R. T. March, and A. D. Rapp, Comparison of stratus cloud properties deduced from surface, GOES, and aircraft data during the March 2000 ARM Cloud IOP, *J. Atmos. Sci.*, *59*, 3256–3284, 2002.

Hahn, C. J., S. G. Warren, J. Gordon, R. M. Chervin, and R. Jenne, Atlas of simultaneous occurrence of different cloud types over ocean, *NCAR Tech. Note, TN-201 + STR*, 212 pp., Natl. Cen. for Atmos. Res., Boulder, Colo., 1982.

Hahn, C. J., S. G. Warren, J. Gordon, R. M. Chervin, and R. Jenne, Atlas of simultaneous occurrence of different cloud types over land, *NCAR Tech. Note, TN-241 + STR*, 211 pp., Natl. Cent. for Atmos. Res., Boulder, Colo., 1984.

Han, Q., W. B. Rossow, and A. A. Lacis, Near-global survey of effective droplet radii in liquid water clouds using ISCCP data, *J. Clim.*, *7*, 465–497, 1994.

Ho, S.-P., B. Lin, and P. Minnis, Estimation of cloud properties over oceans using VIRS and TMI measurements on the TRMM satellite, paper presented at the AMS 5th Symposium on Integrated Observing Systems, Am. Meteorl. Soc., Albuquerque, NM, 15–19 January 2001.

Kropfili, R. A., Cloud physics studies with 8 mm wavelength radar, *Atmos. Res.*, *35*, 299–314, 1995.

Kummerow, C., W. Barnes, T. Kozu, J. Shiue, and J. Simpson, The Tropical Rainfall Measuring Mission (TRMM) sensor package, *J. Atmos. Oceanic Tech.*, *15*, 809–817, 1998.

Lin, B., and W. B. Rossow, Observations of cloud liquid water path over oceans: Optical and microwave remote sensing methods, *J. Geophys. Res.*, *99*, 20,907–20,927, 1994.

Lin, B., and W. B. Rossow, Seasonal variation of liquid and ice water path in nonprecipitating clouds over oceans, *J. Clim.*, *9*, 2890–2902, 1996.

Lin, B., B. Wielicki, P. Minnis, and W. Rossow, Estimation of water cloud properties from satellite microwave, infrared and visible measurements in oceanic environments: 1. Microwave brightness temperature simulations, *J. Geophys. Res.*, *103*, 3873–3886, 1998a.

Lin, B., P. Minnis, B. Wielicki, D. R. Doelling, R. Palikonda, D. F. Young, and T. Uttal, Estimation of water cloud properties from satellite microwave, infrared and visible measurements in oceanic environment: 2. Results, *J. Geophys. Res.*, *103*, 3887–3905, 1998b.

Lin, B., P. Minnis, A. Fan, J. A. Curry, and H. Gerber, Comparison of cloud liquid water paths derived from in situ and microwave radiometer data taken during the SHEBA/FIREACE, *Geophys. Res. Lett.*, *28*, 975–978, 2001.

London, J., A study of the atmospheric heat balance. Final report, Contract AF19 (122)-165, Dept. of Meteorol. and Oceanogr., New York Univ., New York, 99 pp., 1957.

McClatchey, R. A., R. W. Fenn, J. E. A. Selby, F. E. Volz, and J. S. Garing, Optical properties of the atmosphere, 3rd ed., *AFCRL-72-0497*, 113 pp., Air Force Cambridge Res. Lab., Bedford, Mass., 1972.

Minnis, P., P. W. Heck, and D. F. Young, Inference of cirrus cloud properties using satellite-obseved visible and infrared radiance: Part II. Verification of theoretical cirrus radiative properties, *J. Atmos. Sci.*, *50*, 1305–1322, 1993.

Minnis, P., D. P. Kratz, J. A. Coakley Jr., M. D. King, D. Garber, P. Heck, S. Mayor, D. F. Young, and R. Arduini, Cloud Optical Property Retrieval (Subsystem 4. 3, in *Clouds and the Earth's Radiant Energy System (CERES) Algorithm Theoretical Basis Document, Volume III: Cloud Analyses and Radiance Inversions (Subsystem 4), NASA RP 1376*, vol. 3, edited by CERES Science Team, pp. 135–176, Washington, D.C., 1995.

Minnis, P., D. P. Garber, D. F. Young, R. F. Arduini, and Y. Takano, Parameterization of reflectance and effective emittance for satellite remote sensing of cloud properties, *J. Atmos. Sci.*, *55*, 3313–3339, 1998.

Minnis, P., D. F. Young, B. A. Wielicki, P. W. Heck, S. Sun-Mack, and T. D. Murray, Cloud properties derived from VIRS for CERES, paper presented at AMS 10th Conference Atmospheric Radiation, Madison, Wisc., 28 June–2 July 1999.

Minnis, P., D. F. Young, and B. A. Wielicki, Global cloud database from VIRS and MODIS for CERES, paper presented at SPIE 3rd Conference ASIA-Pacific Environmental Remote Sensing, Hangzhou, China, 23–27 Oct. 2002.

Ou, S. C., K. N. Liou, and B. A. Baum, Detection of multilayer cirrus cloud systems using AVHRR data: Verification based on FIRE-II IFO composite measurements, *J. Appl. Meteorol.*, *35*, 178–191, 1996.

Platt, C. M. R., et al., The Experimental Cloud Lidar Pilot Study (ECLIPS) for cloud-radiation research, *Bull. Am. Meteorol. Soc.*, *75*, 1635–1654, 1994.

Poore, K., J. Wang, and W. B. Rossow, Cloud layer thicknesses from a combination of surface and upper-air observations, *J. Clim.*, *8*, 550–568, 1995.

Rossow, W. B., and R. A. Schiffer, ISCCP cloud data products, *Bull. Am. Meteorol. Soc.*, *72*, 2–20, 1991.

Sassen, K., The polarization lidar technique for cloud research: A review and current assessment, *Bull. Am. Meteorol. Soc.*, *72*, 1848–1866, 1991.

Schluessel, P., and W. J. Emery, Atmospheric water vapor over oceans from SSM/I measurements, *Int. J. Remote Sens.*, *11*, 753–766, 1990.

Tian, L., and J. A. Curry, Cloud overlap statistics, *J. Geophys. Res.*, *94*, 9925–9935, 1989.

Uttal, T., and A. S. Frisch, Cloud boundaries during ASTEX, paper presented at the 8th AMS Conference on Atmospheric Radiation, Nashville, Tenn., 23–28 Jan. 1994.

Uttal, T., E. E. Clothiaux, T. P. Ackerman, J. M. Intrieri, and W. L. Eberhard, Cloud boundary statistics during FIRE II, *J. Atmos. Sci.*, *52*, 4276–4284, 1995.

Wang, J., and W. B. Rossow, Determination of cloud vertical structure from upper-air observations, *J. Appl. Meteorol.*, *34*, 2243–2258, 1995.

Wang, J., W. B. Rossow, T. Uttal, and M. Rozendaal, Variability of cloud vertical structure during ASTEX observed from a combination of rawinsonde, radar, ceilometer, and satellite, *Mon. Weather Rev.*, *127*, 2484–2502, 1999.

Wang, J., W. B. Rossow, and Y. Zhang, Cloud vertical structure and it variations from a 20-yr global rawinsonde data set, *J. Clim.*, *13*, 3041–3056, 2000.

Warren, S. G., C. J. Hahn, and J. London, Simultaneous occurrence of different cloud types, *J. Clim. Appl. Meteorol.*, *24*, 658–667, 1985.

Warren, S. G., C. J. Hahn, J. London, R. M. Chervin, and R. L. Jenne, Global distribution of total cloud cover and cloud type amounts over ocean, *NCAR Tech. Note, NCAR/TN-31 7+STR*, 42 pp., plus 170 maps, Natl. Cent. for Atmos. Res., Boulder, Colo., 1988.

Webster, P. J., and G. L. Stephens, Cloud-radiation interaction and the climate problem, *The Global Climate*, edited by J. Houghton, pp. 63–78, Cambridge Univ. Press, New York, 1984.

Wentz, F. J., Algorithm theoretical Basis Document (ATBD): AMSR Ocean Algorithm, *RSS Tech. Rep. 110398*, Remote Sens. Syst., Santa Rosa, Calif., 1998.

Wielicki, B. A., et al., Clouds and the Earth's Radiant Energy System (CERES): Algorithm Overview, *IEEE Tran. Geosci. Remote Sens.*, *36*, 1127–1141, 1998.

Wylie, D. P., W. P. Menzel, H. W. Woolf, and K. I. Strabala, Four years of global cirrus cloud statistics using HIRS, *J. Clim.*, *7*, 1972–1986, 1994.

————————
T.-F. Fan, SAIC, One Enterprise Parkway, Suite 300, Hampton, VA 23666, USA. (t.f.fan@larc.nasa.gov)

S.-p. Ho, Atmospheric Chemistry Division, National Center for Atmospheric Research, P. O. Box 3000, Boulder, CO 80307, USA. (spho@ucar.edu)

B. Lin and P. Minnis, Atmospheric Sciences, NASA Langley Research Center, Mail Stop 420, Hampton, VA 23681, USA. (b.lin@larc.nasa.gov; p.minnis@larc.nasa.gov)